3D shape measurement technique using a printed line pattern

Frederik Allaeys, Geert Luyckx, Christophe Sarrazin, Wim Van Paepegem,
Ljubomir Jovanov and Wilfried Philips
Ghent University
frederik.allaeys@UGent.be

Abstract

The in-house validation of finite element models for bird strike events is currently done by experimental tests on flat plates. High displacement speeds in these experiments demand a small exposure time of the high speed camera (up to 1/50000 s). In order to acquire images of sufficient quality, a special, high-intensity light source has to be used, which is not always possible. The regions with high displacement speeds, therefore, often result in blurry images. In this case, a printed line pattern to estimate the shape of the plate during test provides major advantages over a speckle pattern in terms of reconstruction and optimization of the blurry regions. In this work, a stereo vision technique is developed to reconstructs 3D shape maps using images of impacted plates with printed line patterns. It is shown that two cameras are necessary to calculate accurate shape maps in case of large deflections. The resulting shapes can be used for the validation of numerical simulations.

Keywords: *3D shape measurement, impact, large displacements, line pattern, blurring*

I. Introduction

Experimental verification and calibration tests will always be necessary to validate the assumptions made in numerical simulations. Therefore, measurement techniques need to be developed to determine deflections without interaction with the experiment, e.g. using high speed cameras.

According to the regulations (FAR 25.571) [1], an aircraft needs to be capable of successfully completing a flight after an impact of a 4lb (1.81 kg) bird at cruise speed[1]. In the first series of validation tests, simply supported aluminium plates are used as a target structure and recorded with two Photron high speed cameras. Experiments at such a high speed result in large deformation rates and therefore demand a sufficiently small exposure time to avoid blurring, which is not always possible with the available lighting. A too large exposure time can result in images with blurry regions. Digital image correlation (DIC) is not an option in such situations: for small speckles the correlation between the images drops to unusable low levels with even moderate blur. On the other hand with larger speckles, the localisation accuracy becomes too low.

Techniques for recognition and measurement of 3D structure of motion have received a lot of attention in computer vision, for environment and object recognition and measurement. In this domain, the characteristics of the recorded object such as orientation, shape, amount, etc. are often not known in advance [2]. Here, the stereo vision matching or correlation of the images is done either intensity- or feature-based , making use of edges, corners, curved segments etc. found in

---

[1] Cruise speeds of commercial aircrafts are typically 878-926 km/h

the images.

For experimental mechanics, several techniques besides DIC are available to acquire 3D measurements:

- *Time of flight* methods are based on the time of flight of a laser or other light source pulse [3]; *Laser scanners*, which are active scanners and therefore too slow for experiments with high deformation rates.
- *Electronic Speckle Pattern Interferometry (ESPI)* can measure out-of-plane displacements of rough surfaces with a high degree of precision and accuracy (orders of μm) [4]. Though ESPI can not be used in this case since the resolution of the cameras should be much higher, or the recorded area much smaller.

Several classes of techniques based on line patterns were developed in the past decades:

- *moiré techniques* measure deflections from the interference between two or more superimposed gratings. Geometric moiré or interferometry moiré can accurately measure in-plane displacements, while shadow moiré can measure out-of-plane displacements [5, 6].
- *Fringe projection techniques*, 3D shape maps can also be constructed by projecting a line pattern (fringe projection) on the object [7, 8, 9, 10, 11], using a grating and a light source.

However, shadow moiré and fringe projection techniques have some major drawbacks as they require complete darkness during the experiment and result in low contrast between the dynamic fringes and the background, which is not the case when the line pattern is printed on the object.

Applying a grid of fine lines or a structured pattern of squares to the specimen was already successfully implemented to measure in-plane deformations, 3D shape and strain distributions of a specimen [12, 13]. A grating has the advantage of being distinguishable in two directions, which makes it possible to calculate absolute displacements. But the implementation is less straightforward and the technique is less robust in case of large deflections and rotations.

In this work, a robust algorithm is proposed able to calculate 3D shape maps from specimens during high dynamic events with large displacements using a line pattern printed onto the specimen. It will be shown that due to the large deflections, a stereo vision set-up is necessary to acquire good results.

The next section describes the test set-up. Section three continues with the different necessary steps to calculate the height map: calibration, filtering the line pattern, phase unwrapping and finally the actual shape calculation. Section four presents the results of a verification experiment and the shape map calculation of a bird strike experiment.

II. Experimental set-up

In the first series of validation tests, flat aluminium plates are simply supported onto a thick steel frame with a square opening as represented in Figure 1. The experiment takes place in an evacuated chamber to do precise speed measurements, with several circular windows to record the experiment. The line pattern is applied to the back of the plate and filmed with one or two cameras.

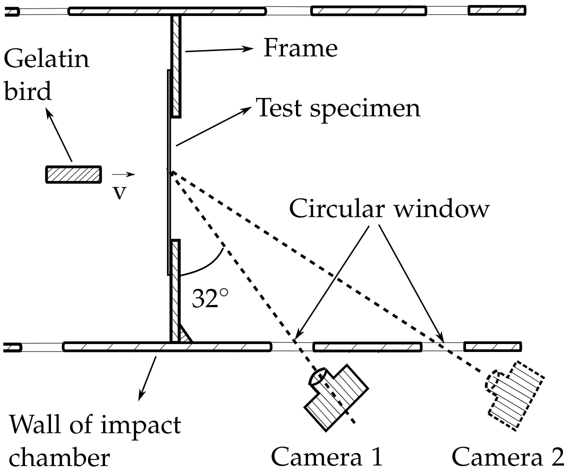

Figure 1: *Principle flat plate tests*

The applied pattern is an equally spaced parallel line pattern (2mm white/ 2mm black). The resolution of the available high speed cameras together with applicable lenses make it possible to acquire eight pixels per line. Generally, depending on the size of the observed specimen, the line pattern and focal length of the lenses can be scaled accordingly.

In the first experiments, the line patterns were applied using pencil and ruler. To improve the accuracy of the method, a flexible polyester stencil was manufactured, which enables more homogeneous application of the pattern with black spray paint. Figure 2 shows the pattern on a plate before impact (left) and just after impact (right). A close-up shows a blurry region due to the exposure time which was too large for the occurring deformation speeds.

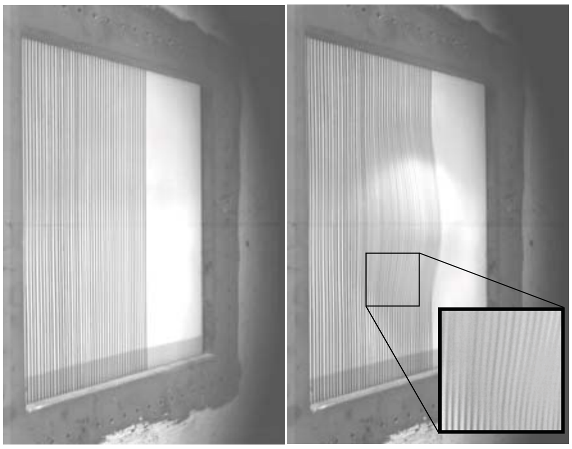

Figure 2: *Line pattern on a deforming plate*

III. Calculation of the height map

This section describes the different steps necessary to calculate the height map. The first step is camera calibration. Next, the line pattern is filtered using contextual filtering, which greatly improves the image quality in blurry regions. In the third step, the lines are uniquely characterized through phase unwrapping. And finally the calculation of the height map is done using one and two cameras.

III.1 Calibration

The camera(s) are calibrated using at least three in-plane and one out-of-plane calibration point. Specifying these coordinates in a world coordinate system and linking them to the corresponding image pixels makes it possible to calibrate the cameras using an iterative minimization method [14].

In this work, a pinhole camera model with negligible lens distortion is assumed. The accurate calculation of the distortion parameters would require a grid or structured pattern in the evacuated chamber, to take the distortion of the circular windows under vacuum into account. To acquire accurate distortion parameters, this grid should be moved in multiple orientations. This would complicate the process too much. Also, the added value of the distortion on the accuracy of the method is relatively small. Taking into account these assumptions, three transformations suffice to project the world (the experiment) on the CCD image (Figure 3): a coordinate transformation (camera rotation and translation) from the world to the camera coordinate system, a central projection on the image plane and a 180 ° rotation of the CCD image.

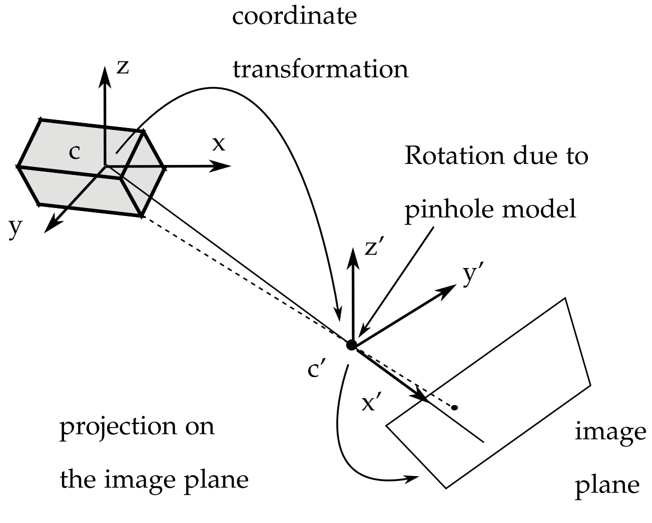

Figure 3: *Transformations from world to CCD coordinates*

The calibration parameters are determined by minimizing the squared differences between the position of the calibration points in the CCD image and the projected corresponding world coordinates on the CCD image, iteratively. Several algorithms exist that are able to minimize the differences. The Nelder-Mead algorithm [15] e.g. is a heuristic algorithm that does not make use of any derivatives. The algorithm starts from an initial simplex[2]. This simplex represents an initial guess of the parameters to be determined. In Matlab specifically, the simplex is constructed using the initial guess plus 5% of each value of the initial guess together with the initial guess itself. Each iterative step, the simplex is modified through several operations (*reflection*, *expansion*, *contraction*

---

[2] A simplex is the *n*-dimensional equivalent of the triangle in 2D. To construct a simplex in a *n*-dimensional solution space, therefore *n+1* values are needed.

and *reduction*) in order to move towards the minimum. A Nelder-Mead algorithm was chosen since it proved to be less dependent on the initial guess or simplex than the Levenberg-Marquardt, the conjugate gradiant and the quasi-Newton algorithm.

The four corners of the square opening of the frame were chosen as in-plane calibration points. For the out-of-plane calibration point, a triangle was mounted next to the square opening. The coordinates of the five points were determined relatively to the centre of the opening at the frontal plane (origin of the world coordinate system). For each experiment, the corresponding pixels in the first image are located after which a Nelder-Mead based algorithm returns the actual position and orientation of the cameras as well as the distance between lens and image centre.

III.2 Filtering of the line pattern

A specific sequence of filters is applied to the images. These filters make it possible to reconstruct lines in blurry regions and eventually makes it easier to calculate the height maps.

The algorithm to reconstruct the blurry regions is based on the work of Hong et al. [16], which proposed contrast enhancement using contextual Gabor filtering for processing finger print images. The algorithm determines the orientation and frequency of the lines locally (by dividing the image in blocks) throughout a normalized image after which a pre-stored Gabor filter is applied.

In this work, the algorithm of Hong is modified to facilitate further processing steps. Solely for the calculation of the orientation and the frequency of the lines, the image is smoothed using a Gaussian filter. The gauss filter eliminates the noise from the image and therefore decreases distortions in the orientation and frequency field. Ratha et al. [17] proposed a method to calculate the orientation map through the gradients, without a singularity at 90° and incorrectly averaged gradients. Therefore the image is firstly divided in blocks of $w \times w$ pixels after which the orientation is calculated in each block (eq. 1).

$$\theta_{block} = \frac{\pi}{2} + \arctan\left(\frac{\sum_{m=-\lceil \frac{w}{2} \rceil}^{\lfloor \frac{w}{2} \rfloor} \sum_{n=-\lceil \frac{w}{2} \rceil}^{\lfloor \frac{w}{2} \rfloor} 2G_x(m,n)G_y(m,n)}{\sum_{m=-\lceil \frac{w}{2} \rceil}^{\lfloor \frac{w}{2} \rfloor} \sum_{n=-\lceil \frac{w}{2} \rceil}^{\lfloor \frac{w}{2} \rfloor} G_x(m,n)^2 - G_y(m,n)^2}\right), \tag{1}$$

where G_x and G_y are the gradients which can be calculated using e.g. the Sobel operator. Hong et al. [16] proposed to apply a low-pass Gaussian filter on each block to eliminate high frequency noise before calculating the orientation. This method did not result in good orientation estimations in the blurry regions (Figure 4a). By smoothing the gradient components G_x^2, G_y^2 and G_xG_y over the entire image the (pixelwise) orientation calculation (eq. 2) proved to be exact as well in the blurry regions, as can be seen in the visualized calculated orientations in Figure 4b.

$$\theta(m,n) = \frac{\pi}{2} + \arctan\left(\frac{2G_x(m,n)G_y(m,n)}{G_x(m,n)^2 - G_y(m,n)^2}\right) \tag{2}$$

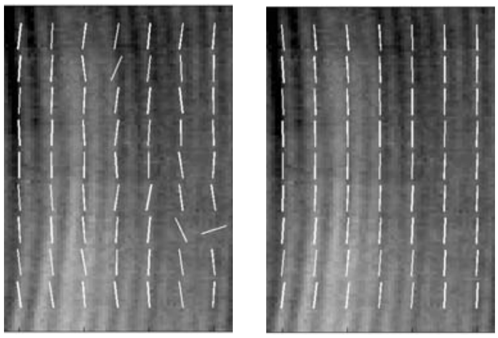

(a) *Method Hong et al. [16]* **(b)** *Proposed pixelwise method*

Figure 4: *Calculated orientation of a line pattern in a blurry region with low contrast*

The method of Hong et al. [16] estimated the line frequency by determining the inverse of the average distance between two consecutive peaks of the x-signature (i.e. the summation of the intensities of each column x of an oriented window). The frequency is assigned to the block corresponding to the rotated window in the image (Figure 5).

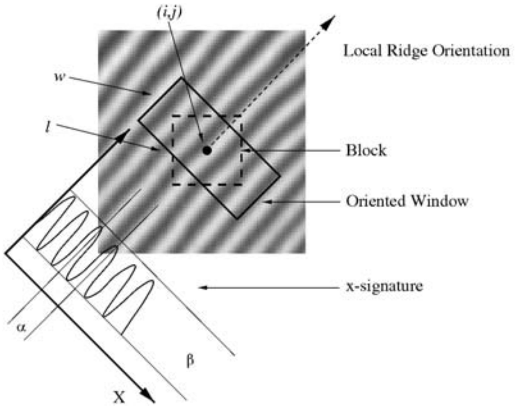

Figure 5: *Oriented window and x-signature*

In order to increase the resolution of the frequency map, the block or region where the frequency is assigned to, can be chosen smaller than the oriented window. This way the block can be smaller than the minimum window needed to calculate the frequency.

Knowing the orientation and frequency of the lines, an adjusted Gabor filter (without DC component) can be applied. The Fourier transform of a Gabor filter is equal to the sum of two Gaussians centered at $\pm 1/\lambda$, where λ represents the wavelength of the sinusoidal factor. As the standard deviations of these Gaussian functions increase, the tails of the Gaussian functions will start to overlap at the origin, resulting in a non-zero DC component. Subtracting a well-chosen Gaussian function from the Gabor filter in the spatial domain, makes it possible to eliminate the DC component and noise in the image in one operation. Equation 3 shows the adjusted Gabor filter in which the DC component is eliminated in the x-direction.

$$n(x,y) = e^{-\pi\frac{x^2+y^2}{\sigma^2}} \cos(2\pi\frac{x}{\lambda}) - be^{-\pi\sigma^2(\frac{1}{\lambda})^2} e^{-\pi\frac{b^2x^2+y^2}{\sigma^2}}, \tag{3}$$

where x and y are the coordinates in a local coordinate system oriented according to the calculated orientation and λ the local line frequency. Figure 6 shows the intensities of a pixel line before and after Gabor enhancement, with and without the DC component. On the bottom of the graph a part of the original image is shown. The pixel line considered in the graph is the one just above the blackened pixel line in the image. The filtered image is an accurate representation of the real pattern. Around 80 pixels, severe distortion occurs in the original signal. The Gabor enhancement without DC component completely reconstructs this region and eases the further processing of the image.

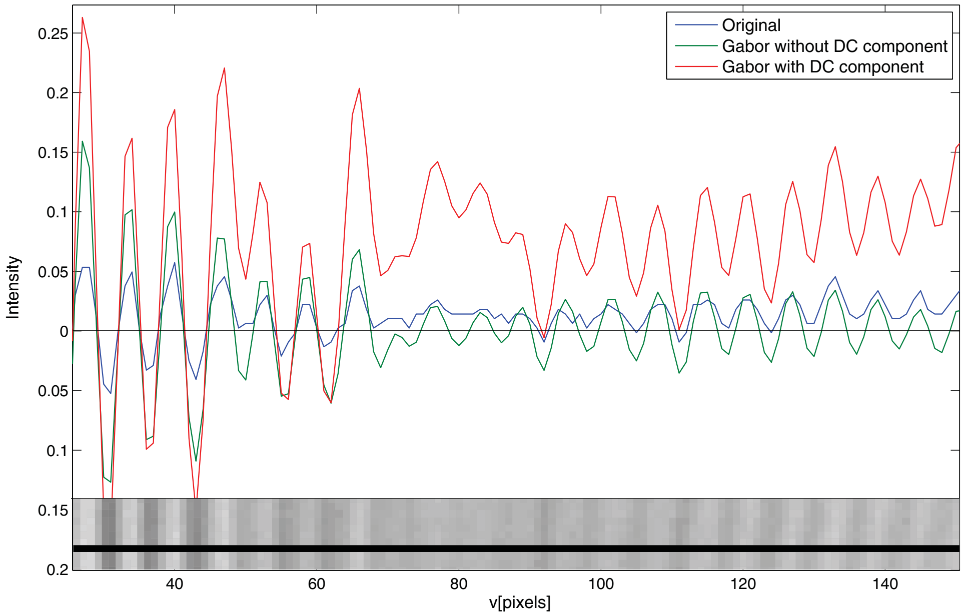

Figure 6: *Intensities of a pixel line before and after Gabor enhancement*

III.3 Wrapped and unwrapped phase

After reducing the noise (high frequency) and background (low frequency) in the original image by means of contextual band-pass filtering, a wrapped phase (between $-\pi$ and π) can be determined. Here, the intensities are transformed to phases. To construct the wrapped phase of the image, all local minima ($-\pi/2$) and maxima ($\pi/2$) are determined. Between these local extrema, the phase in each point is calculated using the intensity of the point and the intensity of the surrounding extrema. In the unreliable regions where the local amplitude is too small between consecutive extrema, the phase is not determined to make sure no lines are lost when the phases are unwrapped.

Unwrapping the wrapped phase is done by calculating a sum of relative phases to construct an absolute phase. Phase unwrapping is the process of adding correct integral multiples of 2π to each wrapped phase value. Unwrapping makes it possible to uniquely distinguish lines from each other.

The key to reliable phase unwrapping is the ability to accurately detect 2π phase jumps. Noise and discontinuities can result in false phase jumps which necessitates an adequate unwrapping algorithm. In this work, a quality-guided flood fill algorithm [18] was used. A special buffer guides the algorithm first through the reliable areas. The first value taken from this buffer is the one with the highest local amplitude in the filtered image. Hence, discontinuities in the unwrapped phase map inherent to blurring only occur in the unreliable areas.

III.4 Calculation of the height map

In case of large deflections, it is necessary to use two cameras for the height map calculation. When using only one camera, deflections need to be calculated by estimating the motion of lines. In this case, an assumption has to be made regarding the direction of this motion. When two cameras are available, it is possible to calculate shape maps more accurately by estimating disparities using two images in the same time frame.

III.4.1 One camera

When only one camera is used, an assumption has to be made regarding the direction of the displacements. The most profound one is assuming that the displacements occur orthogonal to the reference plane (the reference plane is the plane coincident with the plate in its undeformed state or also, the direction of impact). Using this assumption, the deflection can be calculated by matching a deformed image with the reference image. Figure 7 shows a schematic view of the situation.

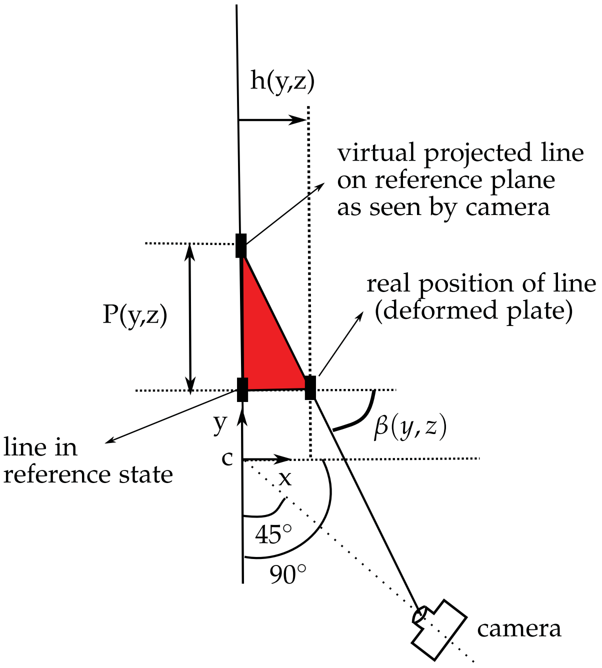

Figure 7: *Principle shape calculation with one camera*

The relation between the shift of the lines $P(y,z)$, the view angle $\beta(y,z)$ and the deflection $h(y,z)$ is the following:

$$h(y,z) = \frac{P(y,z)}{\tan[\beta(y,z)]} \tag{4}$$

III.4.2 Stereo vision

Stereo vision allows constructing deformation maps without using a reference plane. The objective in stereo vision is to match points in one of the images with corresponding points in the other image. Figure 8 shows the principle of the stereo vision technique for shape determination based on triangulation, which does not assume epipolar geometry. Consider a point on a line in the first image plane (camera 1). Every point on the corresponding line in the second image plane (camera 2) represents the same point (since nothing is uniquely distinguishable along the line because of the out-of-plane deformation). In order to find the right corresponding point in the second image, for each point on the corresponding line in the second image, a line is constructed from the point to the pinhole. The point where segment S between the constructed line and the line constructed with the point in the first image is the smallest, is assumed to be the corresponding point. The midpoint of the smallest segment is assumed to hold the correct coordinate of the corresponding points. Since the epipolar condition is not satisfied, the lines are crossing and not intersecting.

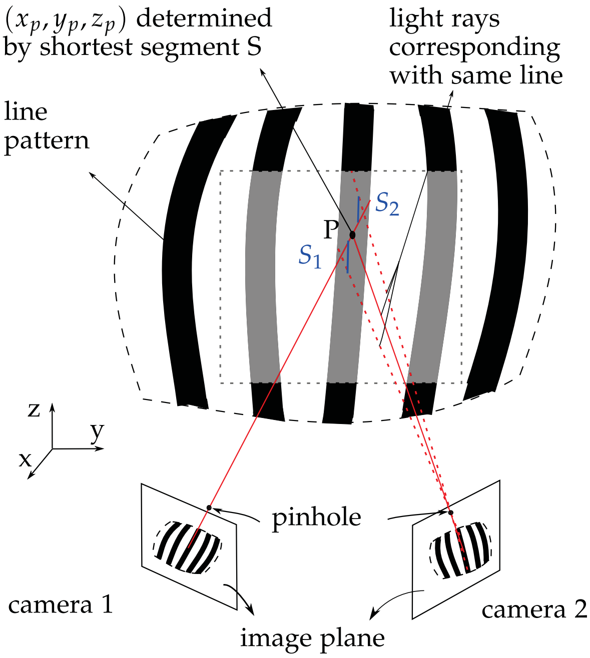

Figure 8: *Principle shape calculation with two cameras*

To eliminate falsely matched points, the segments should be smaller than 1 mm. In order to minimize the calculation time, the algorithm only calculates the segments in the neighbourhood of the previous matched point instead of calculating the segment of all the possible pixels on the corresponding line.

IV. VERIFICATION AND TEST RESULTS

This section starts with a verification of the discussed method, after which a height map calculated from the images of a bird strike experiment is shown.

IV.1 Static calibration test

For the verification, a static calibration set-up was used (Figure 9). In this set-up an aluminium strip was bent through the frame and recorded using two cameras, placed under 32 and 90 degrees.

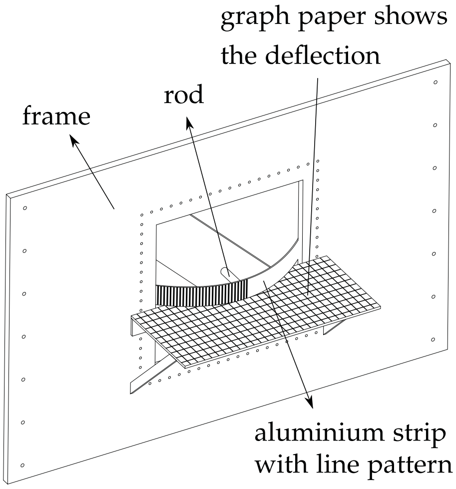

Figure 9: *Static calibration set-up*

A threaded rod was used to push the aluminium strip through the frame. This rod made it possible to consider multiple deflections. For each deflection, the shape of the aluminium strip was drawn on graph paper. Figure 10 shows an image of each camera and a top view of the set-up.

(a) *32°* **(b)** *90°* **(c)** *Top view*

Figure 10: *Image from camera under 45° and 90° and a top view of the set-up*

IV.1.1 One camera

In Figure 11 the deflections calculated using the images of the 32° camera along the horizon are compared with the curves drawn on graph paper.

When the peak displacement is less than 20 mm, the results are good. Unfortunately the deflections commonly seen in bird strike tests with supported plates are much larger. Additionally, since the technique makes use of a reference plane in time (the undeformed state of the plate), a shift of the lines in the y-direction (Figure 7) due to a real shift or rotation of the plate would add up to $P(y,z)$ and would therefore also be seen as a deflection $h(y,z)$. Since the movement of the lines (in the y-direction) in this experiment at $y = 0\ mm$ stays more or less zero throughout the experiment, the assumption of the orthogonal displacements of the lines is valid and therefore, the calculated deflection is accurate in this point. Close to the edge of the frame, the error is large due to the unvalid assumption of the orthogonal deflections. It can be concluded that the use of one camera and a line pattern in case of large 3D displacement fields is not recommended.

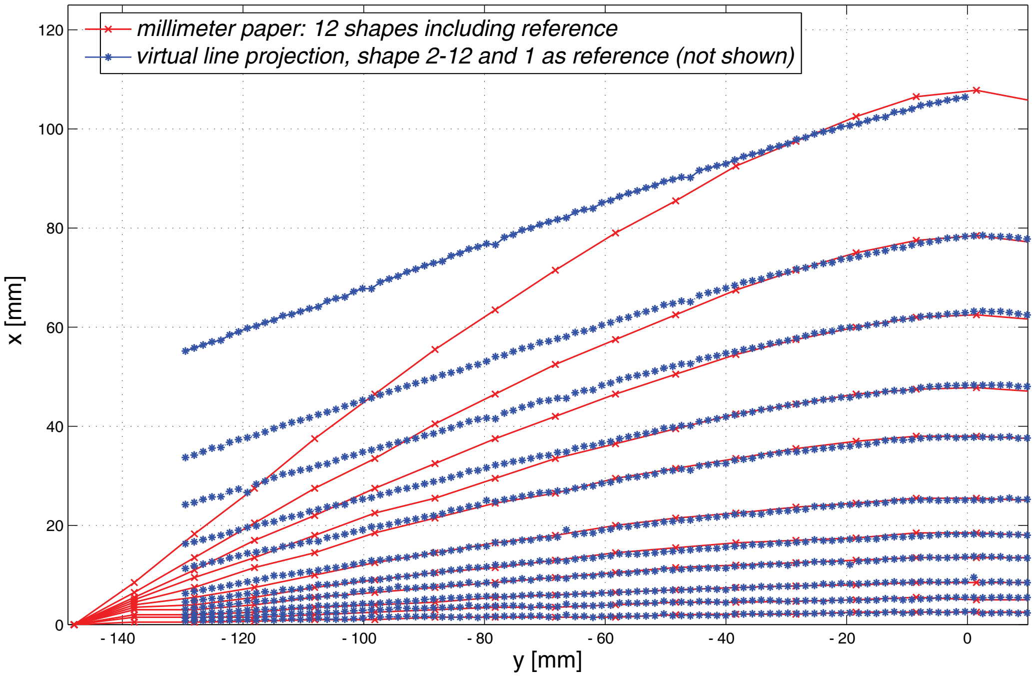

Figure 11: *Calculated deflection profile using one camera*

IV.1.2 Stereo vision

The calculated shape using the images of both cameras agrees well with the experimental evaluation, as can be seen in Figure 12. The maximum error is approximately one millimeter, which will be mainly due to the method of recording the actual shape on the graph paper, but also because of the discretization inherent to digital images.

Choosing a large angle between the cameras improves the accuracy of the method, because it reduces the effect of an error in the process. On the contrary, a large angle decreases the range of orientations of the specimen where the deflection can be calculated. At some point, the orientation of the specimen relative to a camera can become so large that there are not enough pixels anymore to differentiate the lines from each other (Nyguist limit). In order to accurately define the maximum intensity of the lines, a minimum resolution is required. Increasing the resolution further minimizes the error due to the discrete representation of the experiment.

It should be noted that absolute displacements can not be obtained from multiple shape maps and therefore neither strains or stresses can be calculated. The calculation of absolute displacements is not possible with a line pattern, since it is not uniquely distinguishable in the direction of the lines.

IV.2 Bird strike experiment

In the bird strike experiment considered in this paper, a gelatin bird of 1.782 kg was shot at 80 m/s, at a flat 40x40 cm 2mm thick 2024-T3 aluminium plate centered around a 30x30 cm square opening. A 1:4 gelatin to water mixing ratio was used for the bird. The gelatin was moulded in a

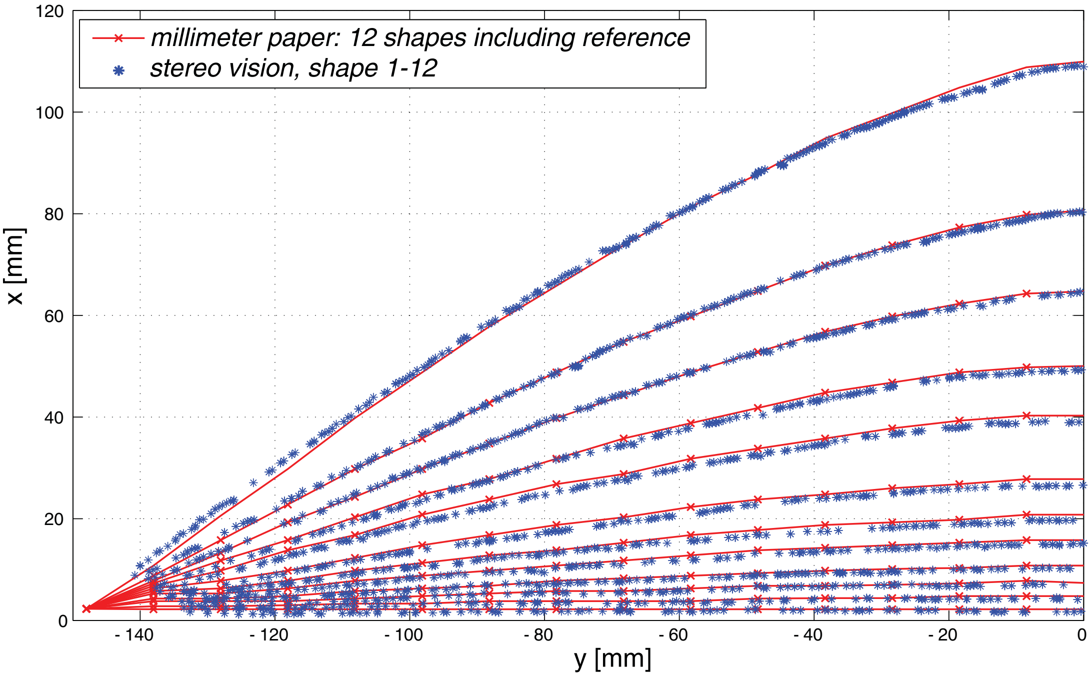

Figure 12: *Calculated deflection profile using two cameras*

cylindrical shape with hemispherical ends and a length over diameter ratio of 1.85. The impact took place approximately 1cm below the centre of the plate. Three high speed cameras were available to record the experiment. Two cameras, a Photron APX-RS and a Photron SA-4 high speed camera with a resolution of respectively 640x848 and 896x752 pixels were used to record the line pattern. A frame rate of 6000 fps was chosen with an exposure time of 1/20000s.

For safety reasons, the second camera could not be placed under 90° (direction of impact). The use of mirrors could make this possible but would introduce additional error into the experiment (a mirror is never entirely flat) and increase the distance to the object and therefore decrease the amount of incoming light. A smaller angle of 58° was therefore obtained. Together with the first camera at 32°, this results in 27° between the two cameras. As stated in IV.1.2, this has consequences on the accuracy of the method. Though 27° is still sufficient to acquire good results and critical boundaries where certainly not met. Figure 1 shows a schematic view of the camera set-up.

Figure 13 shows five frames throughout the experiment with $\Delta T = 0.622ms$. The top row contains the images of the first camera and the bottom row the images from the second camera. The shape map will be calculated for the first four time frames shown in Figure 13 In the subsequent images, a large part of the plate turns black due to insufficient lighting, as shown in the images of the 2.45 ms time frame.

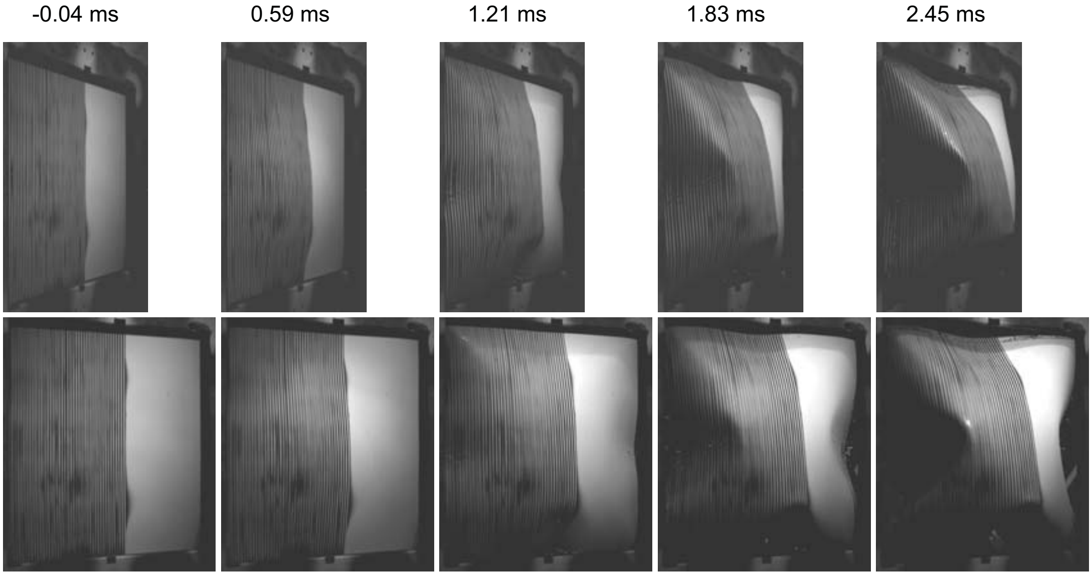

Figure 13: *HSC images from a bird strike experiment in the same time frame (time step: 0.622 ms)*

Figure 14 shows the original image together with the wrapped and unwrapped phase. In case of severe blurring, two lines can be seen as one which inevitably lead to incorrect results. Also, gaps can occur in the wrapped and unwrapped phase map, due to a low local amplitude in the filtered image. Though the gaps are a safety that avoids the calculation of incorrect phases and offsets in the height map.

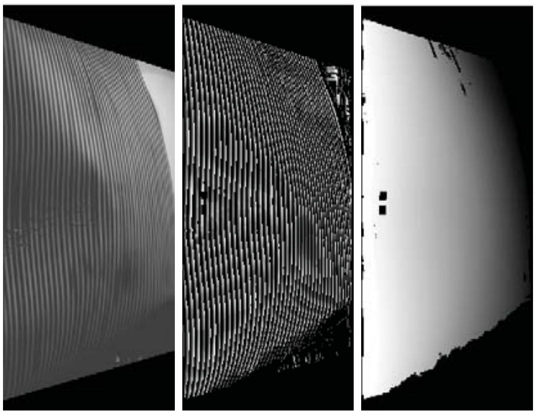

(a) *Original* **(b)** *Wrapped* **(c)** *Unwrapped*

Figure 14: *An original image together with the wrapped and unwrapped phase*

Figure 15 shows the calculated shape maps with a maximum deflection of respectively 3.3, 16.9, 36.9 and 60.2 mm. The deflection in the first time frame is the result of an air pressure wave that precedes the bird. Though it has to be kept in mind that the error on this small value could be relatively large due to the accuracy of the method. The maximum deflection of the last shape map can be found at the top of the bottom dent. The calculated shape maps can tell where the large wrinkles occur in time and how large they are, or in case of damage, at which location it takes place. The dots represent all the midpoints of the segments which are smaller than 1 mm. This way very little noise (falsely matched points) is present in the shape map.

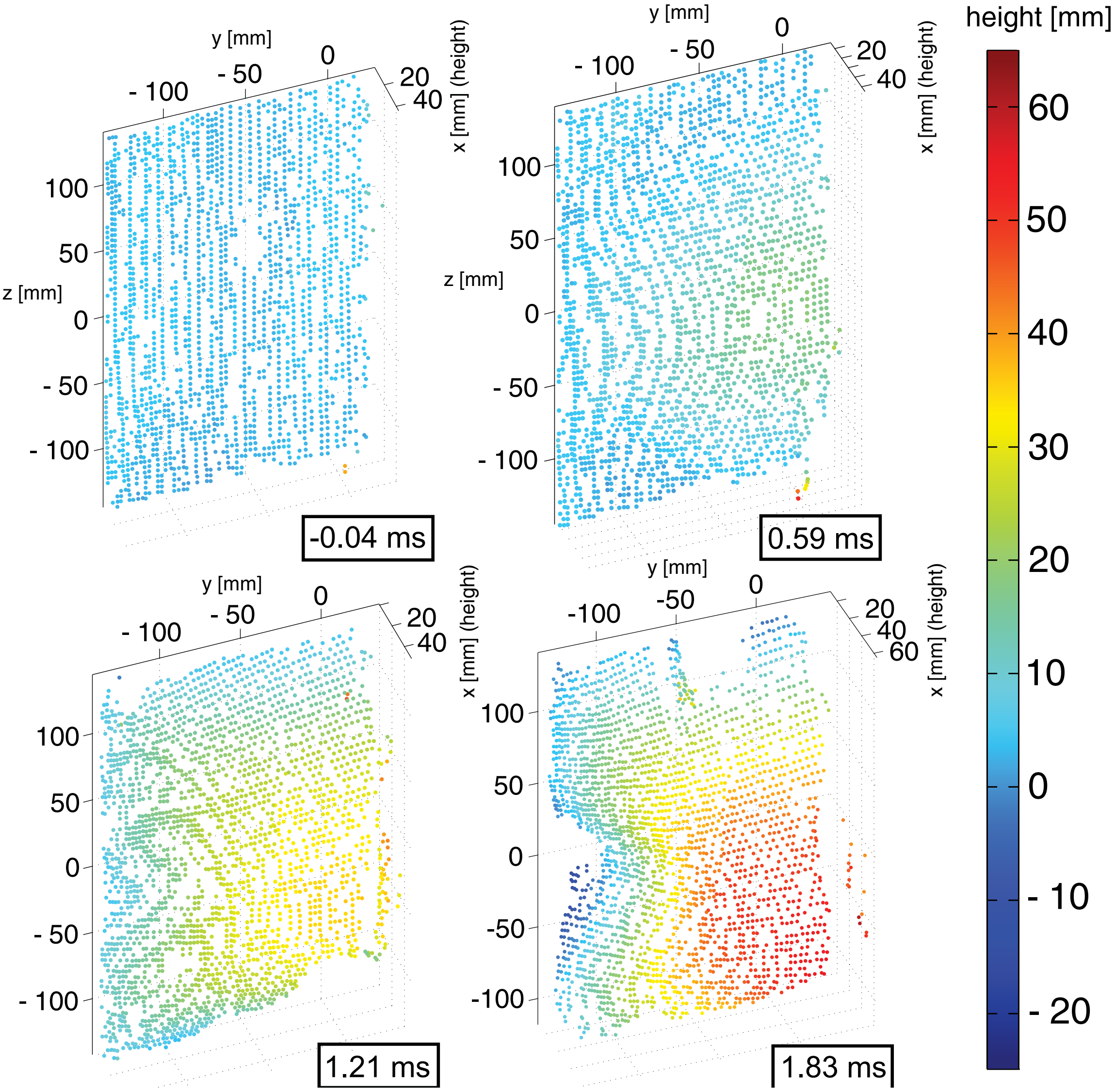

Figure 15: *Calculated deflection profiles of four subsequent images (time step: 0.622 ms)*

V. CONCLUSION

The different steps needed to process the images taken from a printed line pattern and obtain a height map are covered. The main steps are camera calibration, the contextual filtering of the line pattern using adjusted Gabor filters, the construction of wrapped and unwrapped phase maps and finally, the calculation of the height maps in case of one and two cameras. With a static calibration test, the possibilities of using one or two cameras was tested. This was done with a symmetrical set-up. Due to the assumption of orthogonal deflections in case of one camera, the deflection could only be calculated accurately in the centre. Though accurate shape maps could still be calculated for deflections smaller than 2 cm. When two cameras were used, large deflection shape maps were calculated with a maximum error of 1 mm. Finally, the shape of a plate subjected to bird strike was successfully calculated for four subsequent time frames. A maximum deflection of 63.8 mm in the last shape map could be obtained from the results.

Blurring can occur in the recorded images of an experiment due to a combination of high displacement speeds, a high shutter speed and insufficient lighting. The ability to calculate deflection maps from images with mildly blurred regions through reconstruction of the line pattern is the main strength of the proposed method. Furthermore, the different processing steps were chosen to ease the implementation, without deteriorating the accuracy of the method.

The technique is not able to measure absolute displacements and therefore neither the strains and stresses, since a line pattern is not uniquely distinguishable in the direction of the lines. When regions are severely blurred, it might occur that two or even more lines are seen as one, which can result in false phase unwrapping and therefore offsets in the shape map. In the future work we will further investigate improvements of robustness of the method in blurred regions, through improvement of the phase unwrapping algorithm.

VI. Acknowledgements

The authors like to thank Techspace Aero for the cooperation and Asco for providing the flat aluminum 2024 T3 plates used in the experiments. The research leading to these results has received funding from the European Union Seventh Framework Programme FP7/2007-2013 under grant agreement n° ACP2-GA-2012-314366-E-BREAK.

References

[1] Federal Aviaton Administration (2013) Regulations and policies. `http://www.faa.gov/regulations_policies/faa_regulations/`. Accessed 20 June 2013.

[2] Nalpantidis L, Sirakoulis GC, Gasteratos A (2008) Review of stereo vision algorithms: from software to hardware. Int J Optomechatroni 2 (4):435-462. doi:10.1080/15599610802438680.

[3] Chen F, Brown GM, Song M (2000) Overview of three-dimensional shape measurement using optical methods. Opt Eng 39 (1):10-22. doi:10.1117/1.602438.

[4] Carberry MM, Pelegri AA (2000) Out of plane deformation measurements of axially loaded composite materials using electronic speckle pattern interferometry. `http://rutgersscholar.rutgers.edu/volume02/carbpele/carbpele.htm`, (2000).

[5] Han B, Post D. (2008) Geometric moiré. In: William NS Jr (ed) Springer Handbook of Experimental Solid Mechanics. pp 601-626.

[6] Post. D and Han B., Moiré interferometry. In: William NS Jr (ed) Springer Handbook of Experimental Solid Mechanics. pp 627-654.

[7] Su X, Zhang Q (2010) Dynamic 3-D shape measurement method: A review. Opt Laser Eng 48 (2):191- 204. doi: 10.1016/j.optlaseng.2009.03.012.

[8] Gorthi SS, Rastogi P (2010) Fringe projection techniques: Whither we are? Opt Laser Eng 48 (2):133- 140. doi: 10.1016/j.optlaseng.2009.09.001

[9] Van Paepegem W, Shulev A, Moentjens A, Harizanova J, Degrieck J, Sainov V (2008) Use of projection moiré for measuring the instantaneous out-of-plane deflections of composite plates subject to bird strike. Opt Laser Eng 46 (7): 527-534.

[10] Chen LJ, Quan C, Tay CJ and Fu Y (2005) Shape measurement using one frame projected sawtooth fringe pattern. Opt Commun 246 (4-6):275-284. doi: 10.1016/j.optcom.2004.10.079.

[11] Madhuri T, Quan C and Tay CJ (2007) Shape measurement using one frame projected sawtooth fringe pattern. Opt Laser Technol 39(3):453-459. doi: 10.1016/j.optlastec.2005.12.002.

[12] Yang I.H. (1994) Analysis of 3D Shape and Strain Distributions of a Deformable Object Using Stereo Vision. J Mech Sci Technol 8 (2):107-114. doi: 10.1007/BF02953259.

[13] Goldrein HT, Palmer SJP, Huntley JM (1995) Automated Fine Grid Technique for measurement of large-strain deformation maps. Opt Laser Eng 23 (5):305-318. doi: 10.1016/0143-8166(95)00036-N.

[14] Hartley RI, Zisserman A (2004) Multiple view geometry in computer vision. Cambridge University Press, Cambridge.

[15] Lagarias JC, Reeds JA, Wright MH, Wright PE (1998) Convergence properties of the Nelder-Mead simplex method in low dimensions. SIAM J Opt 9 (1):112-147. doi: 10.1137/S1052623496303470.

[16] Hong L, Wan Y, Jain A (1998) Fingerprint image enhancement: Algorithm and performance evaluation, IEEE Trans Pattern Anal Mach Intell 20 (8):777-789. doi: 10.1109/34.709565.

[17]] Ratha NK, Chen S, Jain AK (1995) Adaptive flow orientation based feature extraction in fingerprint images, Pattern Recog 28:1657-1672. doi: 10.1016/0031-3203(95)00039-3.

[18] Chen K, Xi J, Yu Y, Chicharo JF (2010) Fast quality-guided flood-fill phase unwrapping algorithm for three-dimensional fringe pattern profilometry. doi: 10.1117/12.870232